Supporting Online Material for

Bottom-Up Dependent Gating of Frontal Signals in Early Visual Cortex

Leeland B. Ekstrom, Pieter R. Roelfsema, John T. Arsenault,
Giorgio Bonmassar, Wim Vanduffel*

*To whom correspondence should be addressed. E-mail: wim@nmr.mgh.harvard.edu

Published 18 July 2008, *Science* **321**, 414 (2008)
DOI: 10.1126/science.1153276

This PDF file includes:

1.Materials and Methods

All procedures were approved by MGH's Subcommittee on Research Animal Care (Protocol #2003N000338) and MIT's Committee on Animal Care, and are in accordance with NIH guidelines for the care and use of laboratory animals.

Subjects. Two male rhesus monkeys (*Macaca mulatta*; MM1 and MM2, 4-6 kg, 4-5 years old) were prepared for fMRI as previously described and trained for a passive fixation task (*S1*). After the monkeys mastered the task (i.e. they achieved accurate fixation performance within a 2 deg x 2 deg fixation window), 26 intracortical microelectrodes were chronically implanted for electrical microstimulation (EM). Based on anatomical MR images, a craniotomy was performed over the right arcuate sulcus, and the dura mater opened. 26 Teflon-coated microwires (25 μm diameter, 90% platinum, 10% iridium) were manually inserted normal to the cortical surface (*S2*) along the rostral bank of the arcuate sulcus (~2-6 mm deep). Wire tips were beveled and stripped of ~40 μm of Teflon prior to insertion. The dura was then closed and the bone flap replaced. The microwires were soldered to a magnet-compatible connector, which was then encased in dental acrylic (Fig. S1A). A ground electrode was implanted between the skull and muscle and attached to the connector. After surgery, T2-weighted images were collected at 7.0 T (details below) to localize the electrode tips (Fig. S1B). Each electrode was also stimulated outside the scanner during a fixation task to identify the movement fields (MFs) and stimulation threshold of the neurons surrounding the individual electrodes (Fig. S2).

Microstimulation. The EM signal was produced by an eight-channel Digital Stimulator (DS8000, World Precision Instruments), controlled by custom software that also generated visual stimulation. Stimulation trains lasted 250 ms and were composed of biphasic square-wave pulses with a repetition rate of 335 Hz, delivered in a monopolar configuration. Each pulse consisted of 190 μs of positive and 190 μs of negative voltage, separated by 100 μs of zero voltage. The sum of the cables' stray capacitance and the monolithic capacitor array EMI filters in the scanner penetration panel ranged from 5.1 nF to 5.3 nF.

Before each fMRI experiment, the threshold to elicit a saccade was determined inside the scanner for each electrode used by varying the EM amplitude until ~70% of stimulation trains induced a saccade from central fixation. Saccade vectors were calculated to determine the MF of each stimulated FEF site; stimulation was set at ~50% of this behaviorally-defined threshold (*S3*). Also, prior to and after each fMRI session, the impedance of each stimulated channel was measured with a 1V, 100 Hz reference signal to estimate the injected current. For MM1, impedance was 32 ± 4 kΩ, 42 ± 5 kΩ, 54 ± 12 kΩ, and 52 ± 22 kΩ for the 4 electrodes used; for MM2, impedance was 31 ± 16 kΩ, 35 ± 14 kΩ, 48 ± 18 kΩ, and 51 ± 16 kΩ for the 4 electrodes used (mean ± standard deviation across all sessions). Estimated currents for the four FEF electrodes used in MM1 were 38 ± 11 μA, 38 ± 13 μA, 105 ± 32 μA and 178 ± 43 μA and in MM2 28 ± 11 μA, 29 ± 8 μA, 46 ± 14 μA and 88 ± 29 μA (mean ± standard deviation across all sessions). It is noted that the currents needed to evoke saccades with chronic electrodes

may be larger than those with higher-impedance acute electrodes, most likely because of growth of a fibrous barrier between the electrodes and neural tissue (*S4*). Finite element simulation showed that gradient switching during MRI scanning barely induced additional currents (Fig. S13).

Functional MRI acquisition. Functional images were acquired on a 3.0 T head-only scanner with a gradient-echo T2*-weighted echo-planar sequence (55 coronal slices, 64 x 64 matrix, TR = 4 s, TE = 24 ms, 1.25 x 1.25 x 1.25 mm^3 isotropic voxels). Prior to each session, a bolus of Microcrystalline Iron Oxide Nanoparticles (MION; 6-10 mg/kg) in isotonic sodium citrate was injected into the femoral or saphenous vein to increase the contrast-to-noise ratio compared to blood oxygen level dependent imaging (BOLD) (*S1, S5, S6*). A saddle-shaped, radial transmit-receive surface coil (12 cm diameter) was employed.

Functional images for the luminance contrast variation experiment (Fig. 5B) were acquired on a 3.0 T full-body scanner with a gradient coil insert, using a gradient-echo T2*-weighted echo-planar sequence (50 horizontal slices, 84 x 96 matrix, TR = 2 s, TE = 19 ms, 1 x 1 x 1 mm^3 isotropic voxels). A four-channel phased array coil (individual coils 6 cm diameter), with GRAPPA reconstruction (*S7*) and image acceleration factor of 2, and a saddle-shaped, radial transmit-only surface coil (17 cm diameter) were employed. MION contrast agent was again used.

Anatomical MRI acquisition. High resolution, T1-weighted anatomical images were collected on a whole-body 3.0 T scanner for the overlay of functional analyses. Under ketamine-xylazine anesthesia (*S1*), an MP-RAGE sequence (178 sagittal slices, 256 x 256 in-plane matrix, TR = 2.5 s, TE = 4.35 ms, TI = 1100 ms, 0.35 mm^3 isotropic voxels, flip angle = 8°) was used to obtain 9 whole-brain volumes, which were averaged together to improve the signal-to-noise ratio. A single radial transmit-receive surface coil (12.5 cm diameter) was employed.

T2-weighted images were collected from MM1 on a 7.0 T MRI scanner to assess the location of the chronically implanted electrodes in prefrontal cortex. Under ketamine-xylazine anesthesia (*S1*), a turbo spin-echo sequence (22 coronal slices, 256 x 224 in-plane matrix, TR = 3.0 s, TE = 7.7 ms, 0.31 x 0.31 x 1.1 mm^3 voxels, flip angle = 90°) was used to obtain partial brain volumes centered around the arcuate sulcus with a single radial transmit-receive surface coil (4 cm diameter).

EM paradigm. A block design was used with 32 s long epochs and 8-12 epochs per run (or time series) to measure fMRI activations from FEF-EM only (experiment one), from the interaction of FEF-EM and visual stimuli placed inside and outside the MFs of the stimulated FEF sites (experiments two and three), and from the interaction of FEF-EM and visual stimuli inside the stimulated MFs in the presence of distracter stimuli (experiment four). A block design with 24 s long epochs and 20 epochs per run was used in the contrast variation experiment (experiment five). In total, 102 420 functional volumes were collected from MM1 (49 sessions) and 68 128 functional volumes from

MM2 (33 sessions), of which 36 400 and 27 760 volumes (15 sessions in MM1, 11 sessions in MM2) respectively, were used to generate the data shown here. The other sessions were used to optimize the EM paradigm.

In experiments one, two and three, 4 electrodes were stimulated sequentially within a TR (Fig. S5A; inter-stimulation interval between consecutive electrodes, ISI = 1 s; ISI for the same electrode = 4 s), with stimulation held constant throughout a session. For experiment four, 2 electrodes were stimulated twice sequentially within a TR (Fig. S12; ISI = 1 s between consecutive electrodes; ISI = 2 s for the same electrode). For experiment five, one electrode was stimulated twice within a TR (Fig. S5A; ISI = 1 s). In experiments two through five, a pseudo-randomized design with multiple stimulus orders was used. Visual stimulation was presented for 133 ms, followed by 250 ms of combined visual stimulation and FEF-EM and then 617 ms with neither (Figs. S5A and S12). A central fixation point was continuously present and the monkeys performed a passive fixation task throughout each run. Eye positions were monitored at 120 Hz using an infrared pupil/corneal reflection tracking system. Summary statistics of the quality of fixation (% fixation, saccades / min, mean standard deviation of eye position along the x and y eye axes) for each experiment are given in Table S2.

Visual stimuli were projected at 1024 x 768 resolution and 60 Hz refresh rate from a LCD projector onto a translucent screen 52 cm from the animals' eyes. Stimuli for experiments two through four were 3 deg diameter, red-blue sine-wave gratings with a spatial frequency of 0.5 cycles/deg (mean luminance of red = 105.8 cd/m^2 and of blue = 55.8 cd/m^2) moving at 2 deg/s along one of 4 axes (0, 45, 90 and 135 deg). The

background was uniformly gray. In experiment four, 3 distractor stimuli identical to the stimulus presented in the FEF-MF were presented for the same 383 ms duration in the contralateral visual field (two at 9 deg eccentricity and at angles of +/- 49 deg from the horizontal meridian, one at 12 deg eccentricity along the horizontal meridian; Fig. S12B). For experiment five, stimuli were 6 deg diameter, monochromatic, contrast-varied, sine-wave gratings (3, 6 12 and 50% contrast) with mean luminance matched to the background (76.9 cd/m^2); spatial frequency, speed and direction of motion were as above.

Statistical analysis. A voxel-based analysis was performed using SPM99, following previously described procedures to fit a general linear model (GLM) (*S1, S6, S8, S9*). Images were motion-corrected within session and non-rigidly co-registered to each subject's own anatomical template using Match software (*S10*). After sub-sampling to 1 mm^3 isotropic voxels, images were smoothed (Gaussian kernel, σ = 0.67 mm) and registered using Match to MM1's T1-weighted anatomical images. Global scaling, and high- and low-pass filtering were employed prior to fitting the GLM (*S1, S9*).

To account for head and eye movement-related activity, covariates of no-interest from the motion realignment parameters and eye traces were used. Eye traces were thresholded, convolved with the MION hemodynamic response function, and sub-sampled to the TR. To assess the potential effects of eye movements on fMRI activation, we performed a one-way ANOVA on the eye traces to test for any significant differences in % fixation, saccade rate, and eye position along the x and y axes between the pairs of

conditions shown in Table S2. We also plotted the mean eye position aligned to EM onset in these same condition pairs (Figs. S9 and S10).

In experiment two, conjunction analysis (*S11*) was used to identify regions that displayed visually-driven activity and a significant interaction between visually- and EM-driven activity ($p < 0.05$, conjunction). To increase statistical power, we used the main visual effect (that is, VEM + V versus EM + F; see Figs. 3C and S7) in our conjunction analyses. In experiment three, conjunction analysis (*S11*) was used to identify regions that displayed visually-driven activity and a difference in response between congruent (VEM) and incongruent (VEM-I) epochs ($p < 0.05$, conjunction). t-score maps from both monkeys were thresholded [see figure legends for the thresholds used; correction for multiple comparisons was done where noted, using the Family-Wise Error procedures in SPM99 (*S12*)] and overlaid on MM1's T1-weighed anatomical images, which were reconstructed with FreeSurfer (*S13*). Flattened cortical representations were created with Caret using the F99 atlas (http://brainmap.wustl.edu/caret, http://brainmap.wustl.edu:8081/sums/directory.do?id=636032) (*S14*). Retinotopic mapping data previously collected in three animals was warped to MM1's T1 anatomical space to label borders between early visual areas (*S15*).

Activity time courses, scatter plots and activity profiles. Time courses of % change in MR signal (Fig. 1C) were calculated with SPM99 by taking a mean over the local t-score maximum and all supra-threshold voxels bordering the maxima (3-7 voxels total). The borders of 12 visual areas were identified on the flattened cortical representation of MM1

using previous retinotopic mapping data (*S15*) and a Caret Atlas based on previous studies (*S16, S17*). Voxels of interest inside these areas were identified and the % change in MR signal sampled with SPM99 to generate scatter plots (Figs. 3D, 4C, S8, S11) and mean signal change values (Figs. 2, 5). To again increase statistical power, in experiment five we used the main visual effect at 50% contrast (that is, 50% VEM + 50% V versus 0% VEM + 0% V) as a localizer to identify voxels for analysis at all contrast levels. In experiments one through four, the first 2 TR in each epoch were excluded to account for the hemodynamic delay of the fMRI signal; for experiment five, the first 3 TR in each epoch were excluded and an additional TR was appended at the end. Standard error of the mean was calculated over the condition epochs.

Finite Element Simulations. Two-dimensional finite element modeling using FEMLAB was used to simulate the effects of switching the magnetic field gradients and estimate what current could be induced in the electrodes during scanning. A manually-segmented head model was generated from T1-weighted anatomical images and filled in using the conductivity and permittivity of ten materials (muscle, eye, bone, brain, CSF, skin, air, platinum, iridium and copper) (*S18, S19*). One simulation was completed without electrodes, and a second simulation with an electrode in the arcuate sulcus and a sub-cutaneous ground electrode. Current density was calculated by solving Maxwell's equations for a magnetic field of 0.08 T varying sinusoidally at 2.5 kHz along an axis perpendicular to the sagittal plane, simulating a frequency or phase-encoding gradient.

2. Supporting Online Text

Why target the FEF?

The FEF is an ideal initial target for this combination of techniques because: (i) EM of the FEF evokes an easy-to-measure behavioral correlate (saccadic eye-movements), which (ii) allows the determination of exactly what level of stimulation is needed to increase FEF output in a behaviorally relevant manner. (iii) The anatomical connections of the FEF are well characterized; hence, the accuracy of the EM-fMRI results without visual stimulation can easily be validated.

In vivo tractography: areas showing increased fMRI activity in the absence of visual stimulation

EM of specific sub-regions of the FEF increased fMRI activity in several functionally connected regions (*S20-S24*). These sites included (i) ipsilateral areas within the superior temporal sulcus including MST, MT, and STP, LIP, V4, supplementary eye fields (SEF), area 45, area 46, superior colliculus, claustrum, putamen, caudate nucleus and medio-dorsal thalamus, and (ii) contralateral FEF and cerebellum (Figs. S3 and S4, Table S1 for abbreviations). Slightly different patterns of functional activation were observed in the two animals (compare Figs. S3 and S4). This apparent discrepancy is not unexpected though, given that the remote activations are induced by clusters of neurons surrounding the individual electrodes (*S25*) and not the entire FEF, and also that the exact position of electrode implantation within the FEF varied between animals. In addition to this demonstration of accurate and precise *in vivo* tractography, further potential uses of

this novel combination of techniques include: (i) tracing connections *in vivo* from a virtually unlimited number of neighboring regions within a single individual, (ii) guiding simultaneous electrophysiological recordings in multiple functionally connected sites, (iii) guiding (ir)reversible deactivation experiments, and (iv) validating other effective connectivity techniques, such as with diffusion-tensor imaging (*S26*) and dynamic causal modeling (*S27*).

Stability of the chronic EM-fMRI method

Chronically implanted electrodes allowed for repeated stimulation of the same FEF sites and were remarkably stable over time. We were able to elicit virtually identical saccades using similar current thresholds during sessions spanning more than 40 and 28 months in monkeys MM1 and MM2 respectively (see e.g. Fig. 1A). Furthermore, we quantified the overall repeatability of the fMRI activations by calculating three-dimensional spatial correlation coefficients, which ranged from 0.71 to 0.83 for pairs of thresholded full-brain t-score maps ($p < 0.05$, corrected) derived from runs in different sessions or within the same session, respectively. Importantly, we did not observe large aspecific activations in regions not known to be connected to the FEF. The specificity, repeatability and accuracy of EM-fMRI through chronically implanted electrodes show the great potential of this tractography technique, which can be used without the need to sacrifice the subjects.

Interactions driven by negative EM effects

In those voxels in areas V3 and V4 that showed a visually-driven response, FEF-EM in the absence of a visual stimulus caused a reduction of fMRI activity. This reduction was not observed in the presence of a visual stimulus (Figs. 2A and 2C), so that the interaction between FEF-EM and visual stimulation was positive in these areas as well (Fig. 2D).

Effects of eye-movements and induction of phosphenes

We considered the possibility that subthreshold FEF-EM induces eye-movements, which could lead to either a blurred representation or an enhanced representation of the stimuli in retinotopically organized cortex. We performed a one-way ANOVA on eye position (x and y), saccade rate and % fixation during each experiment (Table S2). None of these measures were significantly different ($p > 0.05$) between epochs in the interaction comparison (VEM and F versus V and EM, experiment two; VDEM and V versus VEM and VD, experiment four), specificity comparison (VEM versus VEM-I, experiment three) or the luminance contrast comparison (VEM versus V, experiment five). For the interaction contrast in experiment two, we also plotted mean eye traces in both the x and y directions, aligned to the onset of FEF-EM (Figs. S9 and S10). While some deviation was seen (mostly for MM1), the amplitude of this deviation was small (< 0.25 deg) and there were no time points where a significant difference ($p > 0.05$, corrected for multiple comparisons across time points) was found between the pairs of conditions forming the interaction. Thus, differences in eye-movements between conditions cannot explain the observed modulation of visually-driven activity. A second

concern is that FEF-EM may induce a non-specific phosphene or cue that could lead to enhanced visually-driven activity. Recent work (*S28*), however, showed that EM of the SC in monkeys did not produce a phosphene but rather an apparent shift in attention. This conclusion is supported by the failure to generate phosphenes during TMS of human FEF (*S29*).

Feature specific gating

In motion sensitive areas, such as MT, MST and FST, most voxels were significantly more active in the VEM condition than in the VEM-I condition (Figs. 4C and S11). In object-sensitive regions, such as V4 and TEO, we unexpectedly observed a few voxels that were more active during the incongruent epochs (Fig. S11). One speculative possibility is that FEF stimulation in the presence of a moving stimulus tends to have stronger excitatory effects in motion sensitive areas than in more shape selective regions. Future research might investigate the feature preference of the neurons in the voxels with increased activity in the incongruent conditions and compare it to the feature preference in voxels responding more in the congruent condition.

Ventral area shifts in baseline activation due to FEF-EM

An increase in baseline activation in ventral extrastriate areas due to FEF-EM was observed in MM2 (Fig. S4) but not in MM1 (Fig. S3). That baseline shifts were not consistently observed in these areas (*S30-S32*) may be partly due to the distribution of MFs we obtained, which favored large amplitude saccades. FEF neurons generating

large amplitude saccades are more robustly interconnected with dorsal stream areas than ventral ones (*S22*). This observation therefore suggests that other parts of area FEF or multiple fronto-parietal control areas are also recruited during the deployment of spatial attention.

MR gradient-induced currents

Another concern is that switching of the gradient fields during MRI scanning could induce additional current in the electrodes. First, we simulated the effects of gradient switching using a finite-element model (Fig. S13). Both with and without electrodes present, we found that the induced current density did not surpass the 1.23 A/m^2 threshold needed for axonal activation (20 μm diameter fibers) (*S33*). In the vicinity of the electrode tips, the induced current densities were two to three orders of magnitude below the stimulation threshold. Moreover, we never induced saccadic eye-movements during EPI acquisition while stimulating at 50% of the amplitude needed to generate a saccade (Table S2). This observation shows that any induced currents due to gradient switching must have been less than 50% of the actual injected current.

3. Supporting Online Figures

Fig. S1. Anatomical location of electrodes. **(A)** Schematic illustration of the approximate location of the chronically implanted electrode wires along with a multi-pin connector superimposed on a T1-weighted image (350 μm isotropic voxels). **(B)** T2-weighted image at 7.0T (0.3 mm x 0.3 mm x 1 mm voxels) showing 3 electrodes in the anterior bank of the superior branch of the arcuate sulcus.

Fig. S2. Movement field locations. Example traces of the saccades evoked by supra-threshold stimulation for each of the four electrodes used in MM1 (top) and MM2 (bottom), identifying the movement field of the respective FEF sites and hence the location of the visual stimuli used.

Fig. S3. FEF-EM in MM1. Foci of fMRI activation induced by EM of right FEF in MM1 ($p < 0.05$, corrected). White numbers in the top left corner of each slice indicate the antero-posterior distance in mm relative to the interaural line.

Fig. S4. FEF-EM in MM2. Foci of fMRI activation induced by EM of right FEF in MM2 ($p < 0.05$, corrected). White numbers in the top left corner of each slice indicate the antero-posterior distance in mm relative to the interaural line.

Fig. S5. Visual and microstimulation paradigms. **(A)** In experiment two, 4 stimulation events were used sequentially within a given TR. In epochs of combined visual and EM

stimulation (VEM), a visual stimulus was shown for 133 ms, followed by 250 ms of matched visual and FEF-EM and then 617 ms of no stimulation. Note that the lower time line has an expanded time scale and shows one EM and one visual stimulation event. The same timing paradigm was used in visual-only (V) and EM-only epochs, with either the EM or visual stimulation disabled, respectively. In experiment five, only 1 stimulation event was used, and repeated twice, within a given TR (2 s for experiment five). **(B),** In experiment three, 4 stimulation events were again used sequentially within a given TR. Congruent VEM epochs exactly matched that shown in **(A)**. Incongruent (VEM-I) epochs followed the same timing paradigm, except that the visual stimulus was placed in a non-corresponding FEF movement field.

Fig. S6. Piecewise assembly of the interaction between FEF-EM and visually-driven activity figure. **(A)** Flattened, right occipital cortex (MM1) showing visually-driven voxels only ($p < 0.05$, corrected). Sulci are dark grey (see Table S1 for abbreviations) and white [black] solid lines indicate the representation of the vertical [horizontal] meridian. **(B)** Visually-driven voxels with a positive interaction between visual activity and FEF-EM ($p < 0.05$, conjunction). **(C)** Visually-driven voxels with a negative interaction between visual activity and FEF-EM ($p < 0.05$, conjunction). **(D)** The combination of all three types of voxels, as in Fig. 3C, with green [blue] shading indicating the positive [negative] interaction subpopulation. Some of the green and blue subpopulations appear separate from the yellow-orange visual representations; these

regions are still visually-driven, but at a lower significance threshold ($p < 0.05$, uncorrected) through the conjunction.

Fig. S7. Interaction between FEF-EM and visually-driven activity in MM2. **(A)** 2x2 factorial design (F = fixation only, V = visual stimulation, EM = electrical microstimulation, VEM = visual and electrical stimulation). **(B)** Location and sequence of visual stimuli presented (see also Fig. S5). The red dot close to stimulus 4 is the fixation point. The white dashed line indicates the actual location of stimulus 3, partially overlapping stimulus 1. **(C)** Flattened, right occipital cortex showing voxels that are visually-driven (yellow-orange; $p < 0.05$, corrected), and visually-driven voxels with a positive [negative] interaction between visually- and EM-driven activity (green [blue]; $p < 0.05$, conjunction). Sulci are dark grey (see Table S1 for abbreviations) and white [black] lines indicate representations of the vertical [horizontal] meridian.

Fig. S8. MR signal changes across visual regions. Scatter plots (MM1 and MM2) of voxels in areas V3A, MT, LIP, MST, FST, TEO, TE and STP showing % change in MR signal for V epochs relative to the fixation-only condition (x-axis) and the difference between VEM and EM epochs (y-axis). Color code is as in Fig. 3C (yellow now at $p < 0.05$, uncorrected).

Fig. S9. Average horizontal eye position (MM1) during VEM and F epochs **(A),** and during V and EM epochs **(B)**, which represent the condition pairings in the interaction

analysis (Fig. 3C); **(C)** and **(D)** show the average vertical component during these same epochs. The solid red trace plots mean position and the dashed black lines show +/- SEM across the four electrodes stimulated during the 4 s TR (see Fig. S5A). Traces have been aligned to EM onset (VEM, EM), or the matching time in epochs without stimulation (V, F); total duration of stimulation is indicated by the lower, dark grey bar (250 ms). The upper, light grey bar indicates the period of visual stimulation (VEM, V); visual onset, at -133 ms, is not shown. No significant difference was found between the mean VEM and F trace and the mean V and EM trace at any time point ($p > 0.05$, corrected for multiple comparisons across time points; two sample, two-tailed t-test across all acquired trials).

Fig. S10. Average horizontal eye position (MM2) during VEM and F epochs **(A),** and during V and EM epochs **(B)**, which represent the condition pairings in the interaction analysis (Fig. S7C); **(C)** and **(D)** show the average vertical component during these same epochs. The solid red trace plots mean position and the dashed black lines show +/- s.e.m across the four electrodes stimulated during the 4 s TR (see Fig S5A). Traces have been aligned to EM onset (VEM, EM), or the matching time in epochs without stimulation (V, F); total duration of stimulation is indicated by the lower, dark grey bar (250 ms). The upper, light grey bar indicates the period of visual stimulation (VEM, V); visual onset, at -133 ms, is not shown. No significant difference was found between the mean VEM and F trace and the mean V and EM trace at any time point ($p > 0.05$, corrected for multiple comparisons across time points; two sample, two-tailed t-test across all acquired trials).

Fig. S11. Specificity of FEF-EM induced modulations. Responses of voxels (% MR signal change) in areas V1, V3A, V4, MT, LIP, TEO, TE and STP in the VEM-I epoch (x-axis) and VEM epoch (y-axis) relative to the fixation epoch. Color code is as in Fig. 4B (yellow now at $p < 0.05$, uncorrected; blue at $p < 0.05$, conjunction).

Fig. S12. Visual and microstimulation paradigm with distractor stimuli. **(A)** In experiment four, 2 stimulation events were used sequentially within a given TR and repeated (that is, 1-2-1-2); otherwise the V and VEM epochs matched those in experiment two (Fig. S5A). During epochs with distractors (VD, VDEM, D), 3 contralateral stimuli were presented for the same duration as the single stimulus in the FEF MF. Note that the lower time line has an expanded time scale and shows one EM and one visual stimulation event. **(B)** Location and sequence of visual stimuli presented.

Fig. S13. Finite-element model of current induced in electrodes due to switching of the MRI gradient fields. **(A)** 2-D finite element mesh of sagittal slice of the monkey head, with subcutaneous ground electrode and stimulating electrode positioned in grey matter adjacent to the arcuate sulcus (AS). **(B)** A finite-element solution showing total current density without electrodes. **(C)** A finite-element solution showing total current density in the presence of electrodes. **(D)** Inset [white box in **(C)**] shows the total current density at stimulating electrode tip (CSF = cerebral spinal fluid).

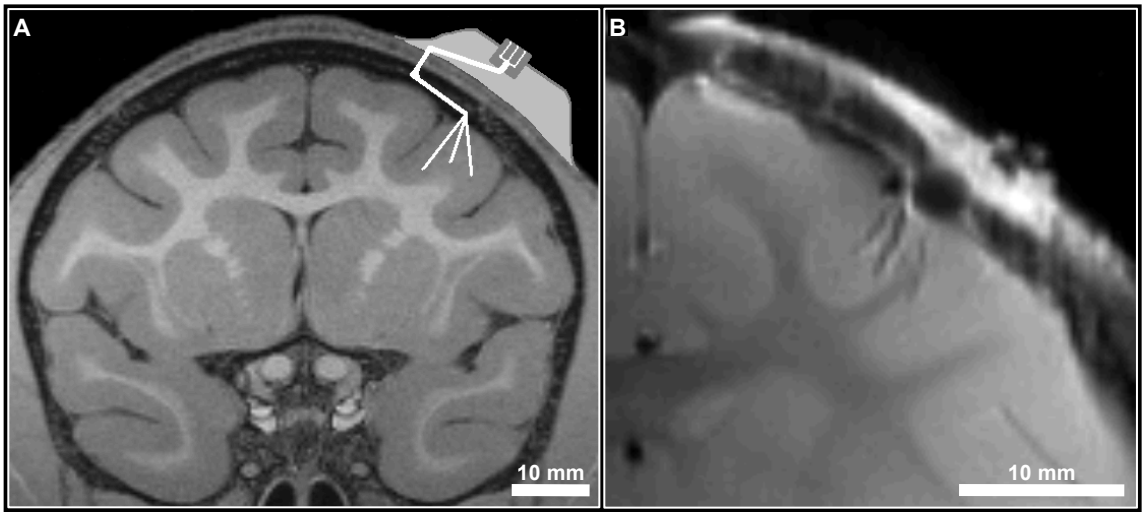

Figure S1

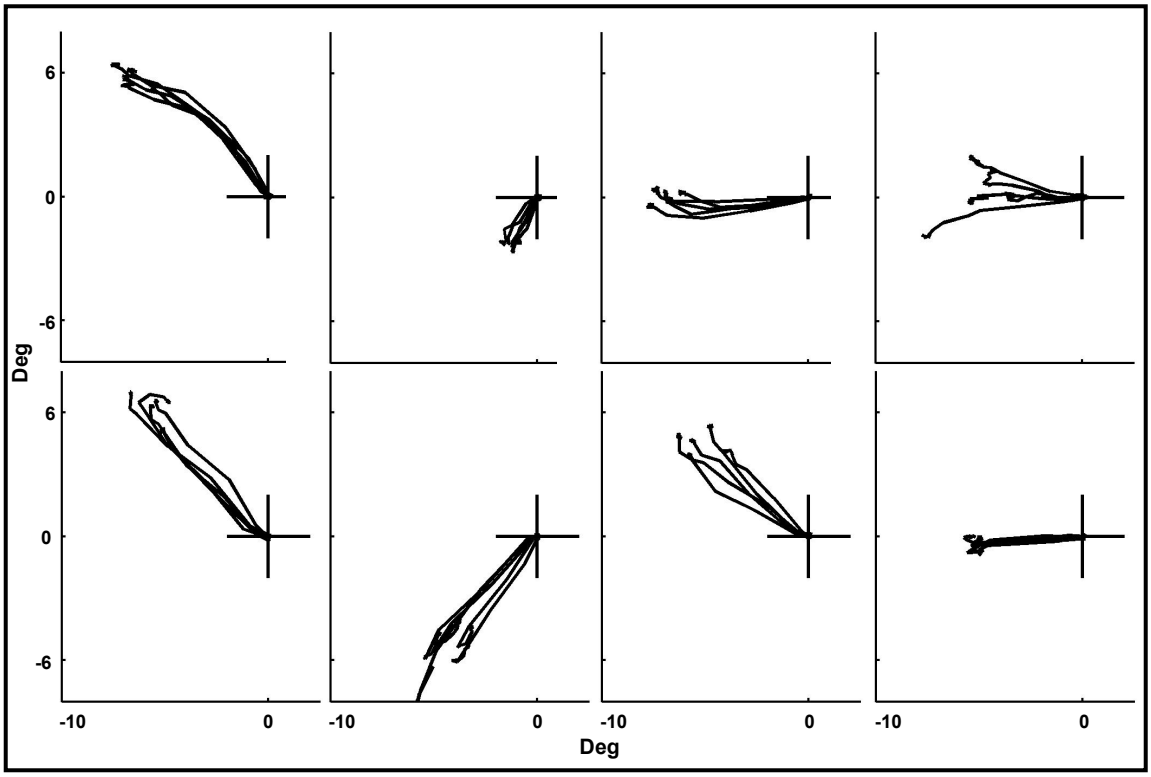

Figure S2

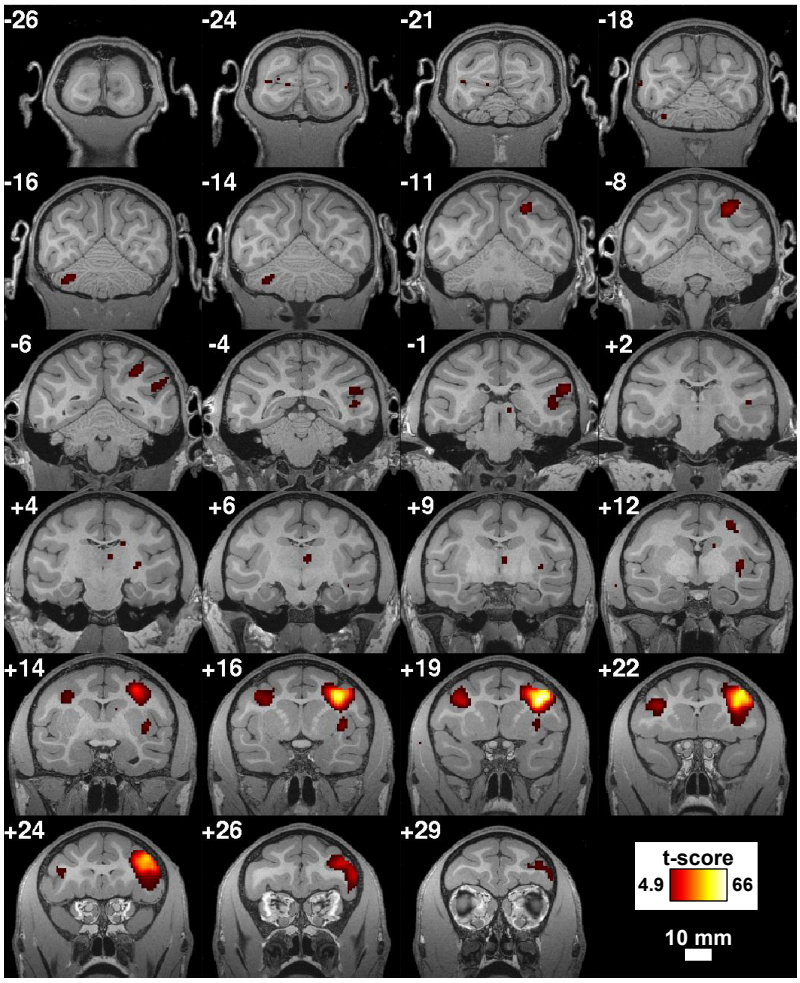
-26
-24
-21
-18
-16
-14
-11
-8
-6
-4
-1
+2
+4
+6
+9
+12
+14
+16
+19
+22
+24
+26
+29
t-score
4.9
66
10 mm

Figure S3

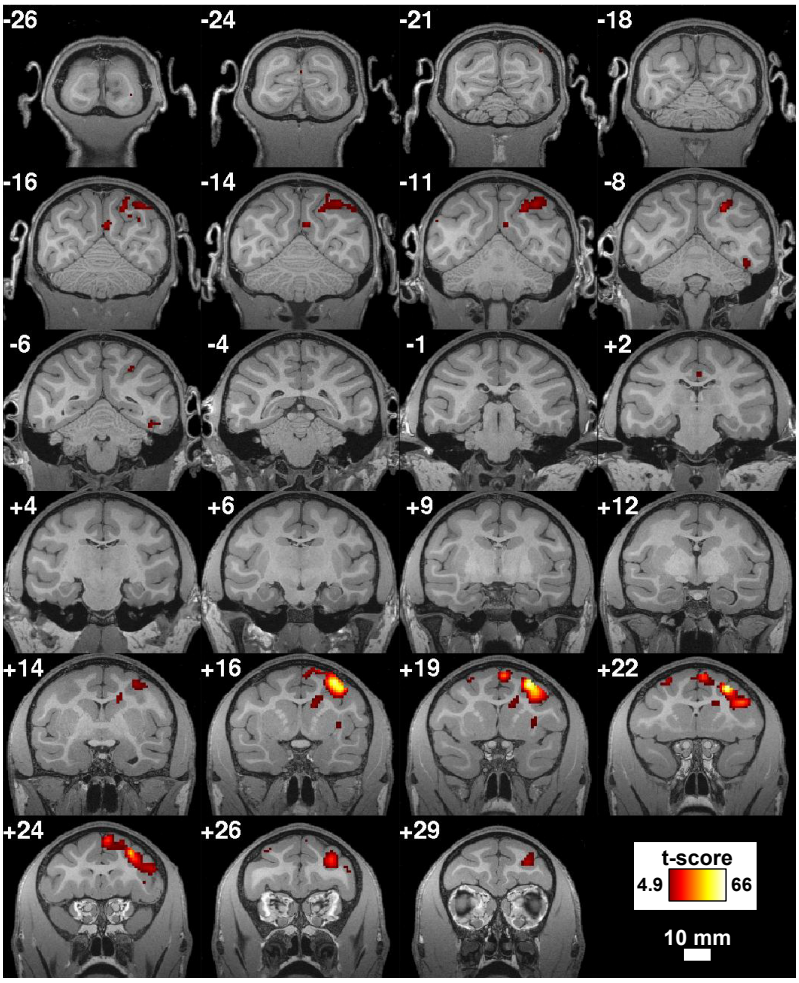
-26
-24
-21
-18
-16
-14
-11
-8
-6
-4
-1
+2
+4
+6
+9
+12
+14
+16
+19
+22
+24
+26
+29
t-score
4.9
66
10 mm

Figure S4

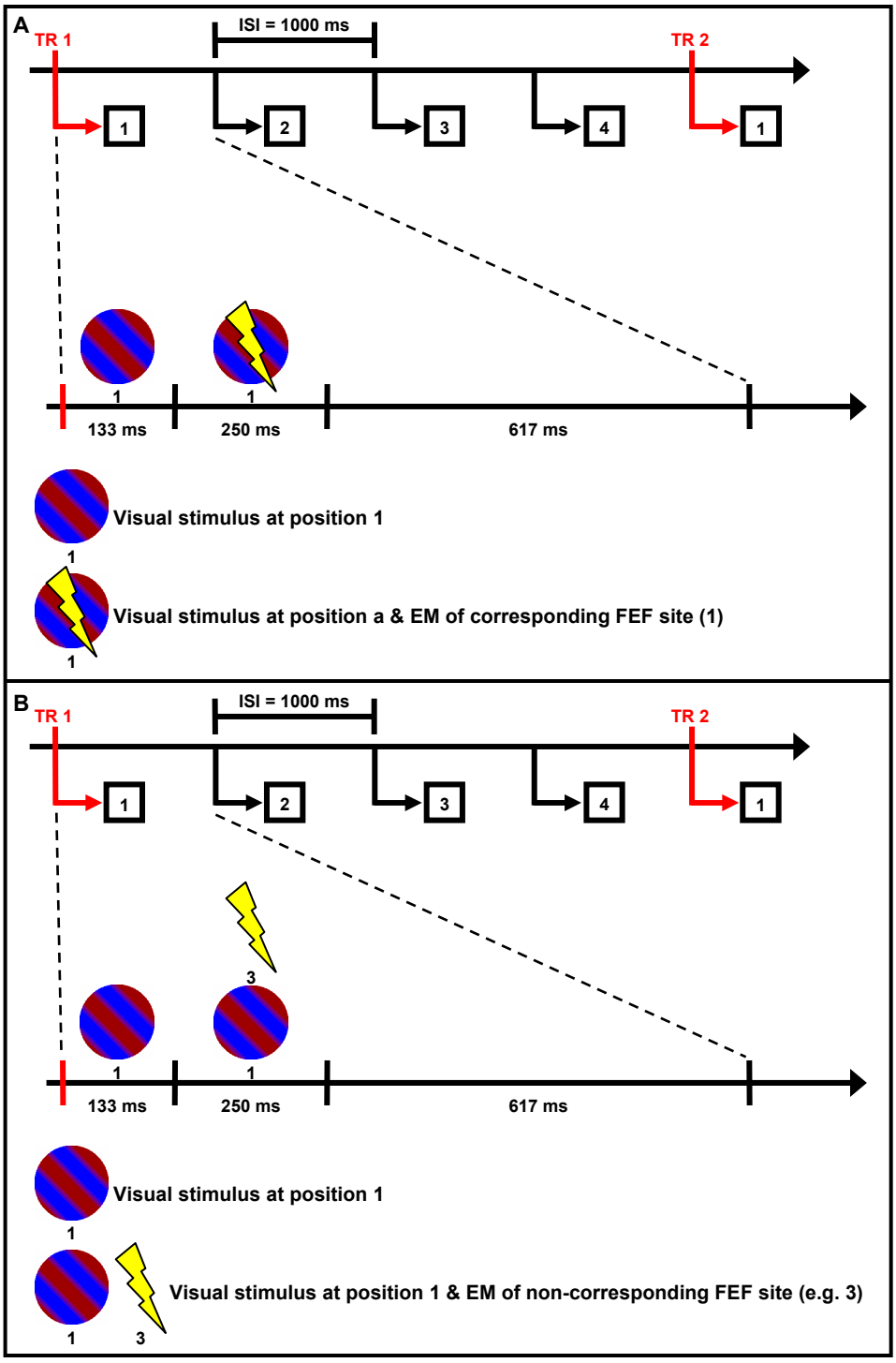
A
TR 1
ISI = 1000 ms
TR 2
1
2
3
4
1
1
1
133 ms
250 ms
617 ms
Visual stimulus at position 1
1
Visual stimulus at position a & EM of corresponding FEF site (1)
1
B
TR 1
ISI = 1000 ms
TR 2
1
2
3
4
1
3
1
1
133 ms
250 ms
617 ms
Visual stimulus at position 1
1
Visual stimulus at position 1 & EM of non-corresponding FEF site (e.g. 3)
1
3

Figure S5

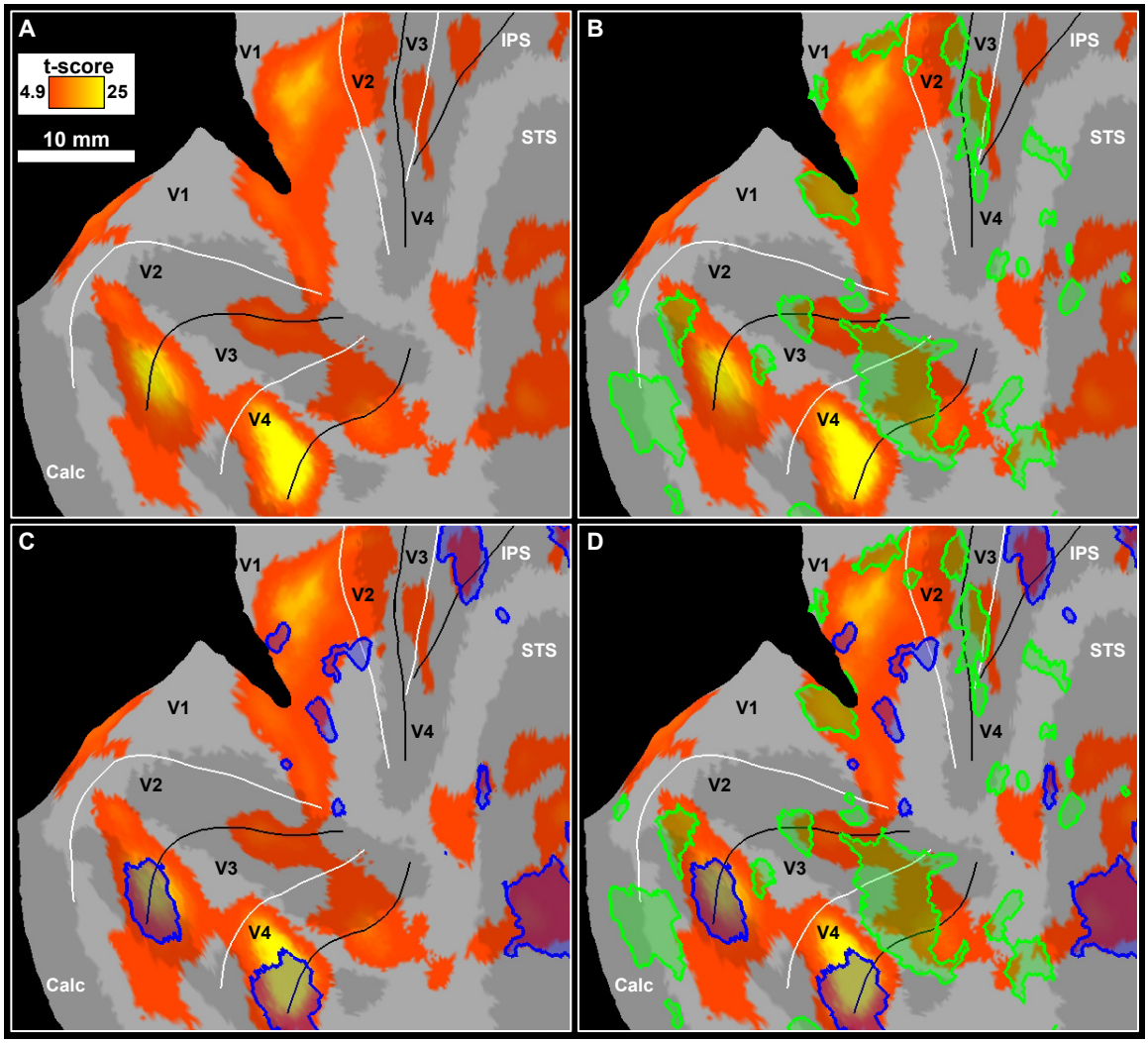

Figure S6

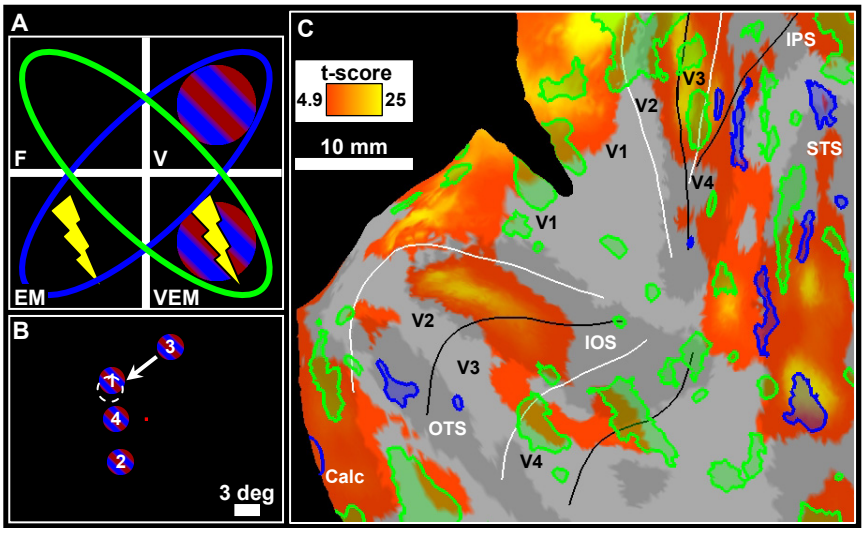
A
F
V
EM
VEM
B
3
1
4
2
3 deg
C
t-score
4.9
25
10 mm
V1
V2
V3
V4
IPS
STS
V1
V2
V3
IOS
OTS
V4
Calc

Figure S7

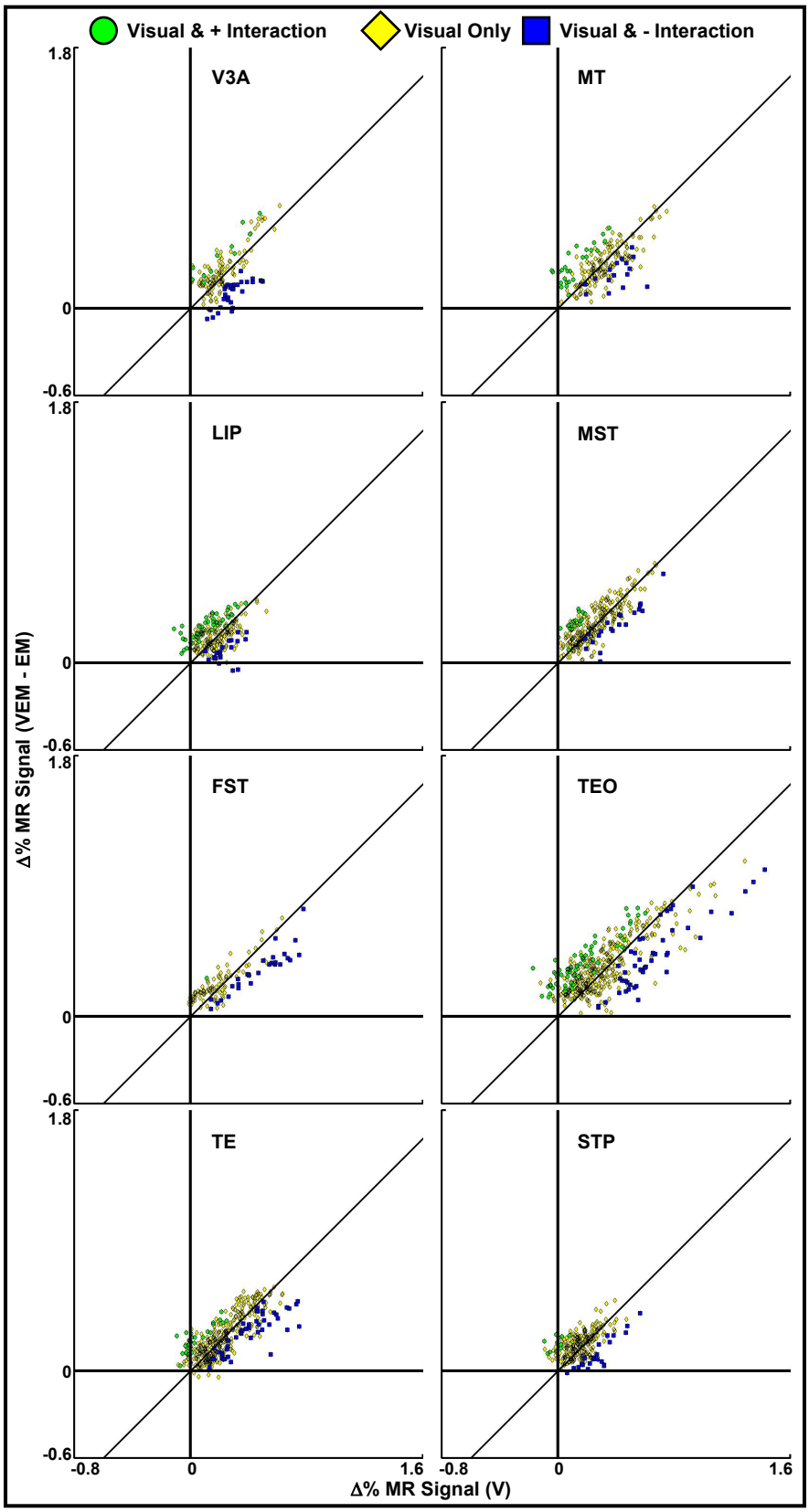
Visual & + Interaction
Visual Only
Visual & - Interaction
V3A
MT
LIP
MST
FST
TEO
TE
STP
1.8
0
-0.6
-0.8
1.6
Δ% MR Signal (VEM - EM)
Δ% MR Signal (V)

Figure S8

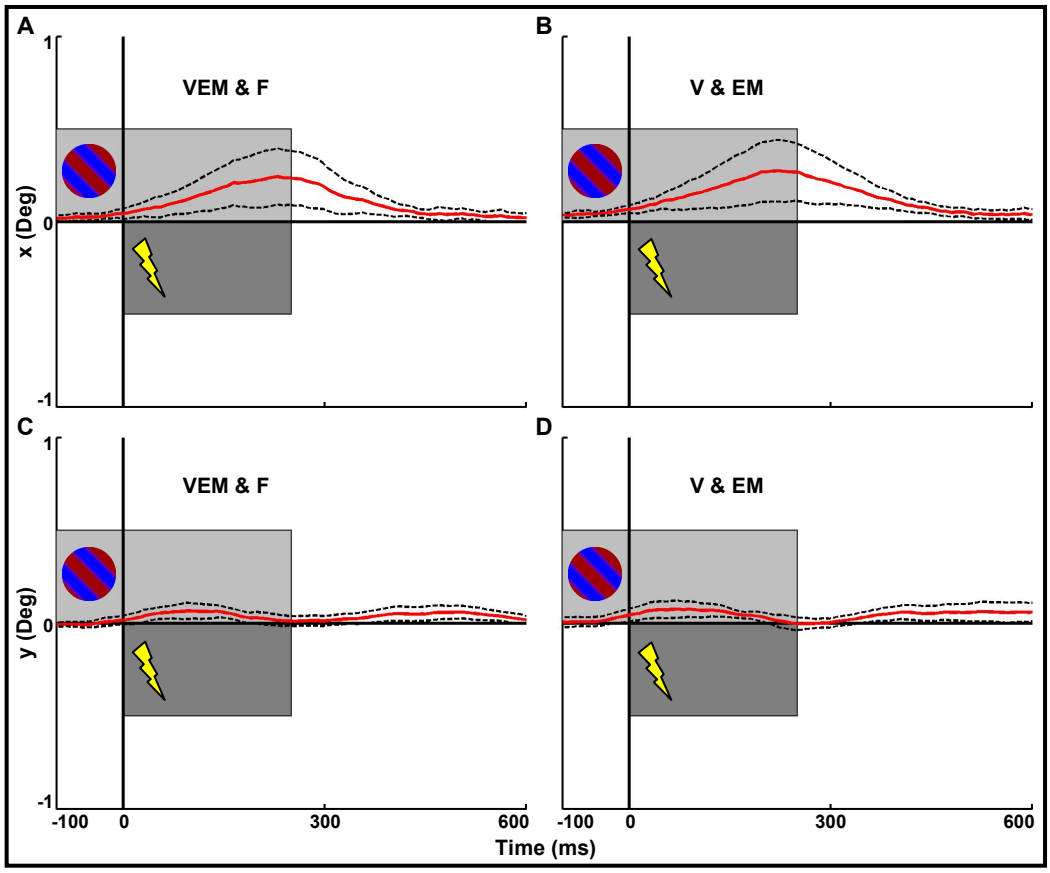

Figure S9

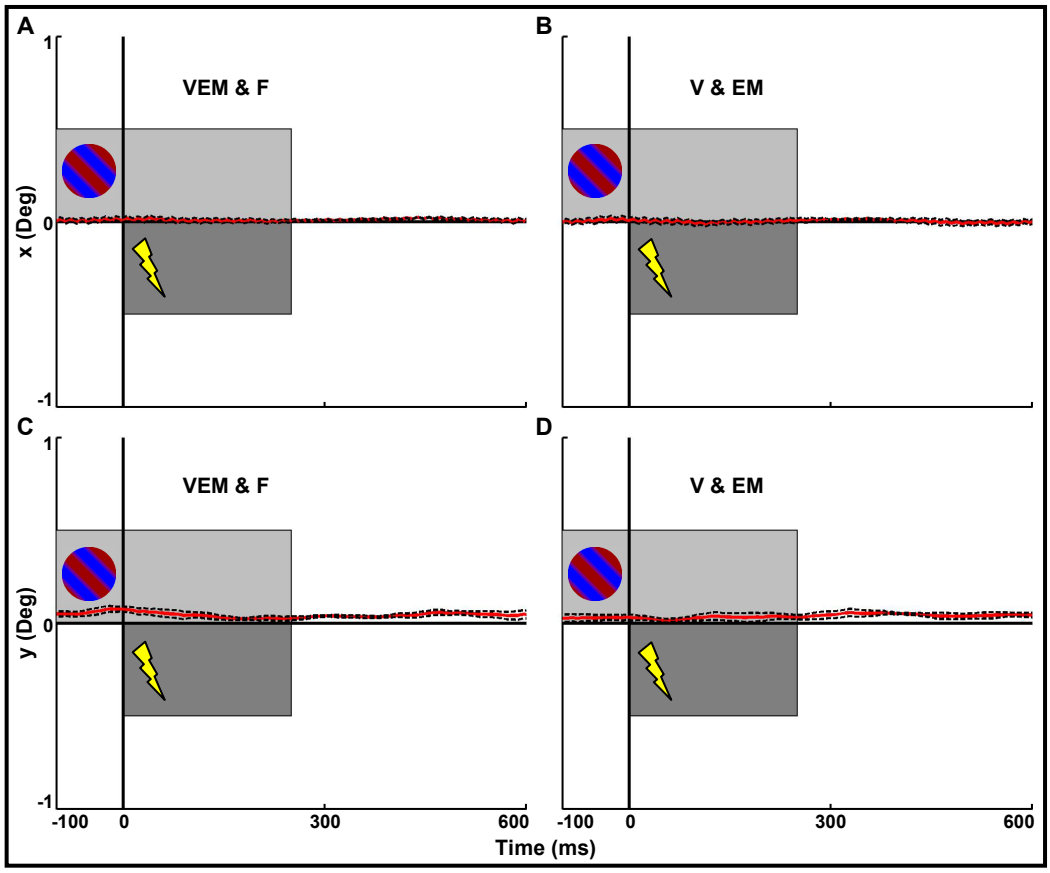

Figure S10

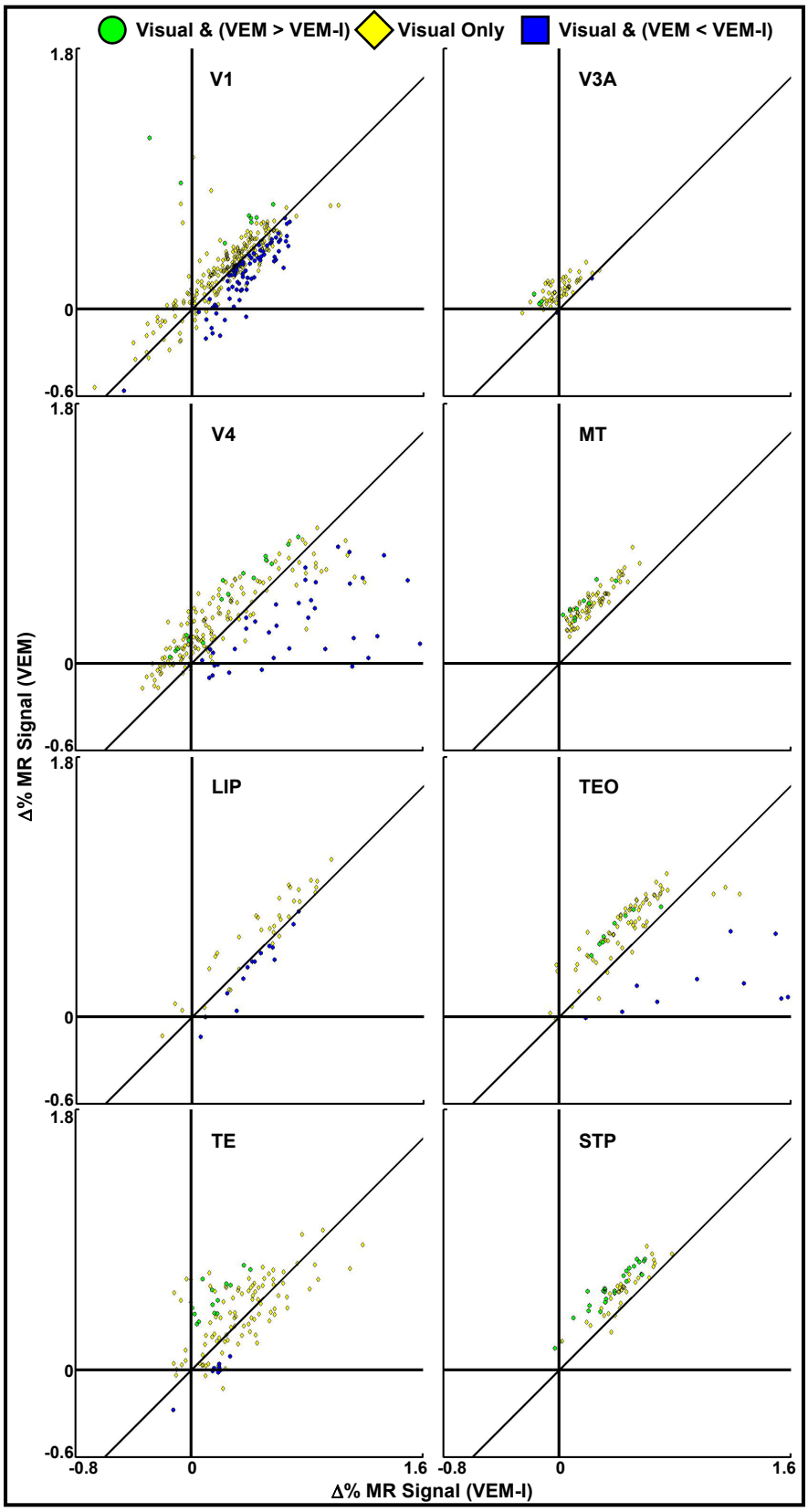
Visual & (VEM > VEM-I)
Visual Only
Visual & (VEM < VEM-I)
V1
V3A
V4
MT
LIP
TEO
TE
STP
1.8
0
-0.6
-0.8
1.6
Δ% MR Signal (VEM)
Δ% MR Signal (VEM-I)

Figure S11

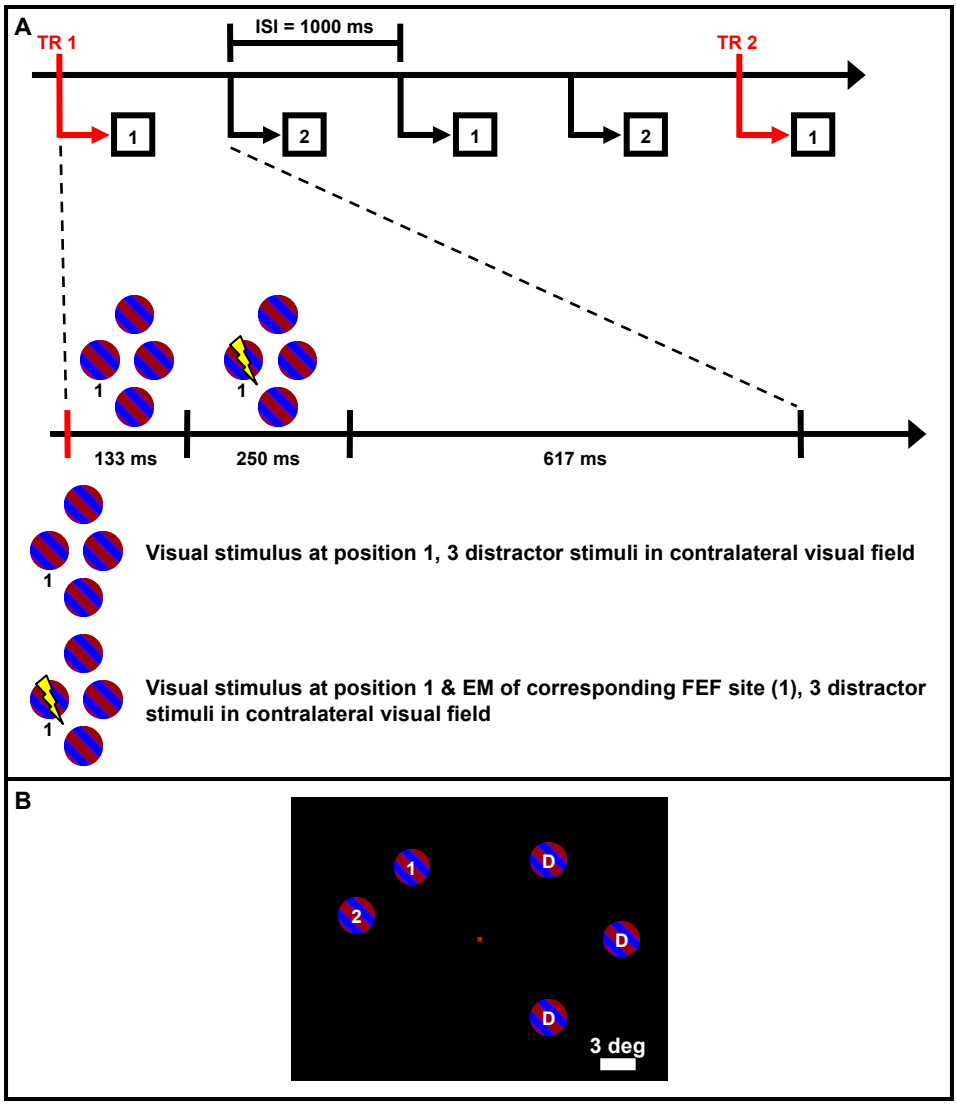
A
TR 1
ISI = 1000 ms
TR 2
1
2
1
2
1
1
1
133 ms
250 ms
617 ms
1
Visual stimulus at position 1, 3 distractor stimuli in contralateral visual field
1
Visual stimulus at position 1 & EM of corresponding FEF site (1), 3 distractor stimuli in contralateral visual field
B
1
D
2
D
D
3 deg

Figure S12

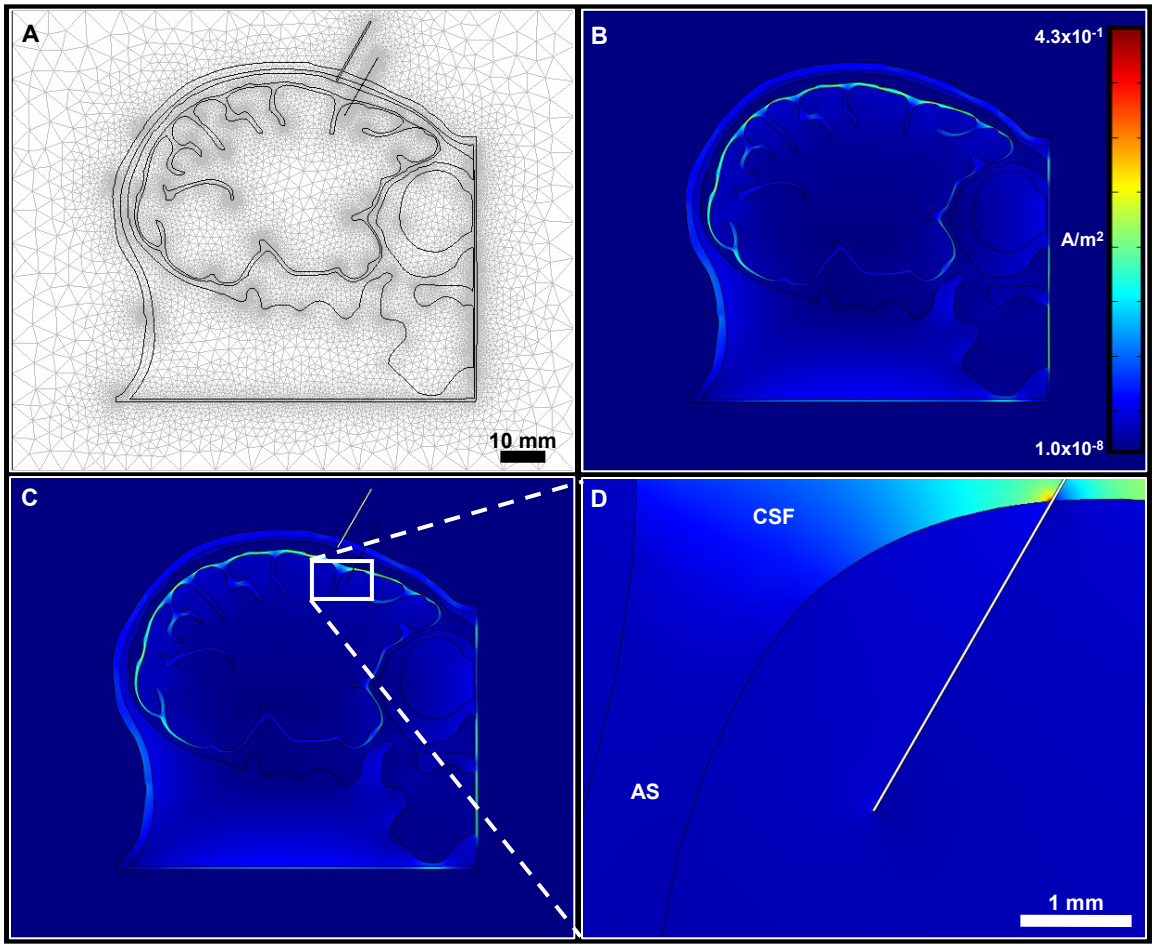

Figure S13

4. Supporting Online Tables

Table S1. Anatomical abbreviations used.

Abbreviation	Meaning	Used in
Calc	Calcarine sulcus	Figs. 3C, S6, S7C
FST	Fundus of superior temporal sulcus	Figs. 2, 4C, S8
IOS	Inferior occipital sulcus	Figs. 4B, S7C
IPS	Intraparietal sulcus	Figs. 3C, S6, S7C
LIP	Lateral intraparietal area	Figs. 1, 2, S8, S11
MT	Middle temporal	Figs. 2, S8, S11
MST	Medial superior temporal area	Figs. 2, 4C, S8
OTS	Occipitotemporal sulcus	Figs. 4B, S7C
SC	Superior colliculus	Fig. 1
STP	Superior temporal polysensory area	Figs. 1, 2, S8, S11
STS	Superior temporal sulcus	Figs. 3C, S6, S7C
TE	Temporal area	Figs. 2, S8, S11
TEO	Temporo-occipital area	Figs. 2, S8, S11

Table S2. Fixation behavior during fMRI runs. n is the number of independent fMRI runs collected for each figure. % Fixation was calculated using a 2 deg x 2 deg window; σ_x & σ_y are the mean standard deviation of eye position along the x & y eye axes, across all repetitions of a condition within a given run. A one-way ANOVA on each condition pair found no significance differences ($p > 0.05$) in any of the distributions.

			% Fixation		Saccades / min		σ_x (deg)		σ_y (deg)	
Figure	**n**	**Conditions**	**Median**	**p**	**Median**	**p**	**Median**	**P**	**Median**	**p**
3C, 3D, S8: MM1	65	VEM + F	94.7	0.51	9.8	0.29	0.13	0.80	0.22	0.83
		V + EM	94.6		9.8		0.13		0.22	
3D, S7, S8: MM2	65	VEM + F	96.0	0.63	7.5	0.32	0.15	0.58	0.22	0.85
		V + EM	96.6		7.5		0.15		0.22	
4, S11	59	VEM	88.8	0.07	13.1	0.81	0.17	0.05	0.28	0.11
		VEM-I	90.9		13.1		0.16		0.27	
5A	53	VDEM + V	93.4	0.48	9.4	0.33	0.15	0.49	0.26	0.47
		VEM + VD	93.3		9.8		0.14		0.27	
5B: MM1	73	VEM	87.5	0.55	9.8	0.44	0.20	0.19	0.34	0.82
		V	86.3		10.3		0.19		0.34	
5B: MM2	88	VEM	87.5	0.33	10.9	0.96	0.25	0.81	0.39	0.69
		V	86.4		11.3		0.25		0.39	

References for Supporting Online Material

1. W. Vanduffel *et al.*, *Neuron* **32**, 565 (2001).
2. L. Mioche, W. Singer, *J Neurosci Methods* **26**, 83 (1988).
3. T. Moore, K. M. Armstrong, *Nature* **421**, 370 (2003).
4. J. R. Bartlett *et al.*, *J Neurophysiol* **94**, 3430 (2005).
5. J. B. Mandeville *et al.*, *Magn Reson Med* **45**, 443 (2001).
6. F. P. Leite *et al.*, *Neuroimage* **16**, 283 (2002).
7. M. A. Griswold *et al.*, *Magn Reson Med* **47**, 1202 (2002).
8. K. J. Friston *et al.*, *Hum Brain Mapp* **2**, 189 (1995).
9. W. Vanduffel *et al.*, *Science* **298**, 413 (2002).
10. C. Chef d'hotel, G. Hermosillo, O. Faugeras, 2002), pp. 753-756.
11. T. Nichols, M. Brett, J. Andersson, T. Wager, J. B. Poline, *Neuroimage* **25**, 653 (2005).
12. K. J. Worsley *et al.*, *Hum Brain Mapp* **4**, 58 (1996).
13. A. M. Dale, B. Fischl, M. I. Sereno, *Neuroimage* **9**, 179 (1999).
14. D. C. Van Essen *et al.*, *J Am Med Inform Assoc* **8**, 443 (2001).
15. D. Fize *et al.*, *J Neurosci* **23**, 7395 (2003).
16. D. J. Felleman, D. C. Van Essen, *Cereb Cortex* **1**, 1 (1991).
17. L. G. Ungerleider, R. Desimone, *J Comp Neurol* **248**, 147 (1986).
18. C. Gabriel, S. Gabriel, E. Corthout, *Phys Med Biol* **41**, 2231 (1996).
19. *CRC Handbook of Chemistry and Physics, 87th ed.* (CRC Press / Taylor and Francis Group, Boca Raton, FL, 2006), p. 724.
20. M. F. Huerta, L. A. Krubitzer, J. H. Kaas, *J Comp Neurol* **253**, 415 (1986).
21. M. F. Huerta, L. A. Krubitzer, J. H. Kaas, *J Comp Neurol* **265**, 332 (1987).
22. J. D. Schall, A. Morel, D. J. King, J. Bullier, *J Neurosci* **15**, 4464 (1995).

23. G. B. Stanton, M. E. Goldberg, C. J. Bruce, *J Comp Neurol* **271**, 473 (1988).

24. G. B. Stanton, C. J. Bruce, M. E. Goldberg, *J Comp Neurol* **353**, 291 (1995).

25. E. J. Tehovnik, *J Neurosci Methods* **65**, 1 (1996).

26. T. E. Conturo *et al.*, *Proc Natl Acad Sci U S A* **96**, 10422 (1999).

27. K. J. Friston, L. Harrison, W. Penny, *Neuroimage* **19**, 1273 (2003).

28. J. Cavanaugh, B. D. Alvarez, R. H. Wurtz, *J Neurosci* **26**, 11347 (2006).

29. C. C. Ruff *et al.*, *Curr Biol* **16**, 1479 (2006).

30. H. J. Heinze *et al.*, *Nature* **372**, 543 (1994).

31. S. J. Luck, L. Chelazzi, S. A. Hillyard, R. Desimone, *J Neurophysiol* **77**, 24 (1997).

32. S. Kastner, P. De Weerd, R. Desimone, L. G. Ungerleider, *Science* **282**, 108 (1998).

33. J. P. Reilly, in *Applied Bioelectricity: From Electrical Stimulation to Electropathology*, (Springer-Verlag, New York, 1998), pp. 105-147.